Two-photon double photoionization of atomic Mg by ultrashort pulses: Variation of angular distributions with pulse length

Roger Y. Bello, ^{1,2} Frank L. Yip, ³ Thomas N. Rescigno, ² Robert R. Lucchese, ³ and C. William McCurdy, ^{1,2} ¹Department of Chemistry, University of California, Davis, California 95616, USA ²Chemical Sciences Division, Lawrence Berkeley National Laboratory, Berkeley, California 94720, USA ³Department of Science and Mathematics, California State University-Maritime Academy, Vallejo, California 94590, USA

(Received 8 July 2020; revised 5 October 2020; accepted 21 October 2020; published 6 November 2020)

We investigate the two-photon double ionization of atomic magnesium induced by ultrashort pulses. Though the initial and final state symmetries are comparable to the same process in helium, in stark contrast the range of photon energies for which nonsequential ionization is the only open pathway is narrow (less than 1 eV) in magnesium. Thus several sequential ionization pathways feature heavily in these processes. Nonetheless, it is found that for pulse durations between 0.25 and 2.0 fs, the joint angular dependence of the ejected electrons can depend sensitively on pulse length, varying between the strictly back-to-back ejection characteristic of nonsequential ionization to other distributions. The significance of excited-state correlating configurations in representing the initial state of magnesium is discussed in the light of their consequences for the resulting angular distributions at photon energies where sequential ionization can access intermediate states that lie nearby in energy, particularly for longer pulses.

DOI: 10.1103/PhysRevA.102.053107

I. INTRODUCTION

Double photoionization (DPI) of an atom or molecule, whereby removal of two electrons via photoabsorption is accomplished, provides a direct means of investigating the consequences of electron correlation in fundamental systems. For years now, both ab initio theoretical investigations and sophisticated coincidence experiments have been conducted on a variety of targets with at least two electrons to eject into the continuum. Examination of the resulting energy sharing and angular distributions (including in the body frame of a molecule) reveals the signatures of electron correlation in both the initial and final states that are fundamental to the nature of matter.

With the advent of intense light sources capable of producing ultrashort pulses, attention has shifted to consider few-photon absorptions initiating the double ionization in the weak-field regime. For these processes, one usually examines two distinct energy regimes towards the double continuum: nonsequential processes whereby the sum total energy of the photons is above that which binds the two electrons to the target, but where neither photon possesses an energy sufficient to remove an electron from both the target and its intermediate ion state, and the sequential regime where the latter conditions are true.

In many regards, these two regimes define different pathways where the role of electron correlation manifests itself in distinct ways based on whether the two photons must act in concert nonresonantly on the initial state (nonsequential) or whether the process can occur by the first photon photoejecting an electron and the resulting intermediate ion absorbing the second photon to remove the other electron (sequential).

Several studies have examined how these different processes impact the features of the single differential cross section (SDCS), which exhibits the characteristics of the energy sharing of the excess energy between the outgoing electrons [1-5]. Additionally, analysis of the angularly-resolved triple differential cross section (TDCS) illustrates that the nonsequential regime results can exhibit signatures of electron correlation more so than the sequential processes [5]. Indeed, the latter can largely be modeled by two independent (i.e., uncorrelated in the final states) photoionization events superimposed on top of each other, whereas for the former such a model fails seriously.

The simplest system to study atomic double photoionization, particularly where the distinguishing features of the sequential and nonsequential domains mentioned above were first explained, is helium; good agreement between experiment and theoretical formulations has led to a better understanding of the double photoionization dynamics than for any other target. In addition to continuing investigations on helium [6], recent work has sought to further advance double ionization investigations by examining heliumlike systems, with several theoretical calculations approximating atomic targets that have ns² valence configurations to be removed by the action of one or several photons [7–12]. Numerous theories have been adapted for studying alkaline earth targets for comparison with theoretical and experimental results for helium by treating these targets using quasi-two electron methods. The appropriateness of these approximations is justified by the large energetic and spatial separation between the core electrons and those in the valence shell that are removed by photoabsorption. Extension of these investigations to other targets that parallel the valence structure of helium in the initial and final states has further elucidated the nature of the electron correlation between the outgoing electrons and illustrated the impact that symmetry considerations, like the common 1S_0 initial state has on the resulting double ionization dynamics.

Beyond recent single-ionization studies examining atomic magnesium [13–16], both theory and experiment have examined double ionization from the valence shell of atomic magnesium by absorption of a single photon [11,12,17,18]. Particular interest has been paid to examining the results of one photon interacting with the $3s^2$ outer electrons at an energy of 55.49 eV, where the transition energy for reaching this part of the double ionization continuum coincides with a resonant process for single-electron promotion from an inner shell, namely the $2p \rightarrow 3d$ transition. Still, within the framework of treating the valence electrons of atomic magnesium in a twoactive electron framework, the theoretical studies mentioned above helped contextualize the experimental measurements on a more complicated helium-like target. Prior theoretical work for two-photon double ionization of Mg examined the energetic consequences for the outgoing valence electrons [19]. In order to extend those results, we have here examined two-photon photoabsorption processes for doubly ionizing the valence electrons of Mg, including the angular distributions of the ejected electrons.

As in our previous work, the formalism we employ to study two-photon absorption processes involves representing and accounting for the interaction of the neon-like core electrons with the valence electrons that will interact with the field in a time-dependent framework. These core electrons influence the outer $3s^2$ electrons via closed-shell Coulomb and exchange interactions whose effect at large distances screens the nucleus. Thus, asymptotically, the problem has much in common with the helium case, where the manner in which the double ionization amplitudes for two-photon absorption are calculated is particularly efficient in that propagation of the wave function need only occur for the duration of the pulse, after which the field-free dynamics can be resolved at any particular final total energy E (as described below, see also [20]). Additionally, our methods for propagation of the wave function have been streamlined to remove the highest kinetic energy spectral components without impacting the physical results, facilitating compact radial grids and greater computational efficiency in representing the action of the pulse.

Inclusion of interactions of the outgoing electrons with the core electrons is facilited here by the construction of a basis of atomic orbitals using an underlying radial grid (here, a finite element discrete variable representation, FEM-DVR [21]). This transformation into an atomic orbital basis spanning only the radial range of the inner-shell core electrons allows for their representation as fixed-occupancy electrons in a configuration interaction (CI) expansion [18,22–27].

In Sec. II, we summarize the representation of the magnesium target wave function in this orbital-grid basis and review the extraction of the double photoionization amplitudes from a propagated pulse interaction by solving a driven Schrödinger equation that effectively resolves the field-free dynamics in the $t \to \infty$ limit for a particular final state energy E. In Sec, III, we examine the results for two-photon ionization of magnesium, where sequential processes dominate the

two-photon regime because of a very narrow nonsequential region. Section IV provides some conclusions.

II. THEORETICAL FRAMEWORK

A. Wave-function expansion

The method for combining the two-active electron approximation with numerical grids and exterior complex scaling (ECS) to study the double photoionization from multi-electronic targets has been previously described in detail [18,22–27]. Thus here we provide only a brief description of the essential ideas. Atomic units are used throughout the following, unless otherwise stated.

The two-active electron representation of the magnesium target relies on the frozen-core approximation, involving a full configuration interaction (CI) of $3s^2$ valence electrons in the presence of the $1s^22s^22p^6$ (frozen) core. Within this approximation, the Mg wave function is expanded as linear combination of spin adapted configurations (omitting the spin variables),

$$\Psi(\mathbf{r}_1, \mathbf{r}_2) = \sum_{ij} C_{ij} |1s^2 2s^2 2p^6 \zeta_i(\mathbf{r}_1) \zeta_j(\mathbf{r}_2)|, \qquad (1)$$

where the functions $\zeta(\mathbf{r})$ are products of a primitive radial DVR function [21] and a spherical harmonic, and the inner shells $1s^22s^22p^6$ electrons are held fixed in the expansion configuration. The energetic gap between the valence and core electrons and the close-shell character of the core electrons make this approximation reasonably valid. Accordingly, the Hamiltonian of the $3s^2$ electrons is effectively

$$H = h(1) + h(2) + \frac{1}{r_{12}},\tag{2}$$

where $1/r_{12}$ represents the interaction between the valence electrons and the one-body Hamiltonian in Eq. (2) can be formally written as

$$h = T - \frac{Z}{r} + \sum_{o} (2J_o - K_o), \tag{3}$$

where T is the one-electron kinetic energy operator, -Z/r represents the nuclear attraction (for magnesium, Z=12), and the terms in the sum over occupied orbitals, $2J_o$ and K_o represent the direct and exchange interactions of the $1s^22s^22p^6$ frozen-core with the valence electrons, respectively. The direct operator for the nl closed-shell orbitals is

$$J_{nl}(\mathbf{r}) = \int \frac{|\varphi_{nl}(\mathbf{r}')|^2}{|\mathbf{r} - \mathbf{r}'|} d\mathbf{r}', \tag{4}$$

while the nonlocal exchange component, defined based on its operation on the orbital $\zeta(\mathbf{r})$, is given by

$$K_{nl}(\mathbf{r})\zeta(\mathbf{r}) = \varphi_{nl}(\mathbf{r}) \int \frac{\varphi_{nl}^*(\mathbf{r}')\zeta(\mathbf{r}')}{|\mathbf{r} - \mathbf{r}'|} d\mathbf{r}'.$$
 (5)

The nl closed shell orbitals defining the direct and exchange operators in Eqs. (4) and (5) are the 1s, 2s, and 2p Hartree-Fock orbitals of neutral magnesium. The diagonalization of the Hamiltonian in Eq. (2) provides the ground state energy and initial state wave function of the valence electrons.

The frozen-core energy, which is common to both bound and continuum states, can be regarded as a global energy shift, since it is constant with respect to expansion coefficients in Eq. (1).

To represent these operators, as well as both the bound and continuum wave functions on a radial grid, we have used a modified finite element discrete variable representation [22]. Accounting for the occupancy of the core orbitals requires the construction of atomic orbitals out of the underlying FEM-DVR radial basis,

$$\varphi_{\alpha}(r) = \sum_{i=1}^{M} U_{\alpha j} \chi_{j}(r), \tag{6}$$

where the radial atomic orbital basis φ_{α} is expanded in FEM-DVR radial functions, χ_{j} , via a unitary transformation matrix $U_{\alpha j}$. The transformation in Eq. (6) need only to be done in the region where the orbitals describing the core electrons are significantly different from zero. Beyond that region and, in particular, over the radial distances necessary to describe ionization processes, the primitive FEM-DVR basis is untransformed. Consequently, a fundamental point in the transformation is that the basis orbitals φ_{α} together with the long-range primitive FEM-DVR functions χ_{j} , are mutually orthonormal.

B. Two-photon double ionization amplitudes

The interaction of the atomic target with the radiation pulse is described by solving the time-dependent Schödinger equation (TDSE),

$$i\frac{\partial}{\partial t}\Psi(t) = \mathcal{H}(t)\Psi(t),$$
 (7)

where $\mathcal{H}(t) = H + V_t$, with H being the atomic Hamiltonian in Eq. (2) and V_t is the laser-atom interaction. Using the length gauge and within the dipole approximation the laser-atom interaction is given by $V_t = \mathbf{E}(t) \cdot (\mathbf{r}_1 + \mathbf{r}_2)$, where the electric field for a photon of energy ω and total duration T can be written as

$$\mathbf{E}(t) = \begin{cases} E_0 F_{\omega}(t) \hat{\epsilon}, & t \in [0, T], \\ 0, & \text{elsewhere,} \end{cases}$$
 (8)

where E_0 is the maximum electric field amplitude and $\hat{\epsilon}$ is the polarization vector. We have chosen a sine-squared envelope for the time dependence of the pulse $F_{\omega}(t)$,

$$F_{\omega}(t) = \sin^2\left(\frac{\pi}{T}t\right)\sin(\omega t). \tag{9}$$

In order to resolve the asymptotic form of the wave packet long after the action of the laser pulse, we follow the arguments in Refs. [5,20,28–30]. We compute the scattered wave function at a specific total energy E within the bandwidth of the pulse by solving the (time-independent) driven equation

$$(E - H)\Psi_{rc}^{+}(\mathbf{r}_1, \mathbf{r}_2) = \Psi(\mathbf{r}_1, \mathbf{r}_2, T), \tag{10}$$

with the wave packet at the end of the pulse $\Psi(\mathbf{r}_1, \mathbf{r}_2, T)$ taken as the driving term. The correct outgoing boundary conditions for both single and double ionization are imposed on $\Psi_{sc}^+(\mathbf{r}_1, \mathbf{r}_2)$ in Eq. (10) by applying the ECS transformation [21,31–37] to the radial coordinates of both electrons, scaling

those coordinates by a complex factor $e^{i\theta}$ beyond some radius \mathcal{R}_0 ,

$$r \to \begin{cases} r & \text{if } r \leqslant \mathcal{R}_0 \\ \mathcal{R}_0 + (r - \mathcal{R}_0)e^{i\theta} & \text{if } r > \mathcal{R}_0 \end{cases} . \tag{11}$$

The extent of the real part of the grid \mathcal{R}_0 must be large enough to contain the spreading wave-packet during the propagation, avoiding unphysical reflections off the grid boundaries. To understand how the amplitudes for the different channels can be extracted from Ψ_{sc}^+ , we note that the wave packet at the end of the pulse can be formally decomposed into all of the energetically open channels as

$$\Psi(\mathbf{r}_{1}, \mathbf{r}_{2}, T)$$

$$= \psi_{\text{bound}}(\mathbf{r}_{1}, \mathbf{r}_{2}) + \psi_{\text{single}}(\mathbf{r}_{1}, \mathbf{r}_{2}) + \psi_{\text{double}}(\mathbf{r}_{1}, \mathbf{r}_{2})$$

$$= \psi_{\text{bound}}(\mathbf{r}_{1}, \mathbf{r}_{2}) + \sum_{n} \int dk_{n}^{3} C(\mathbf{k}_{n}) \psi_{k_{n}}^{-}(\mathbf{r}_{1}, \mathbf{r}_{2})$$

$$+ \int dk_{1}^{3} \int dk_{2}^{3} C(\mathbf{k}_{1}, \mathbf{k}_{2}) \psi_{k_{1}k_{2}}^{-}(\mathbf{r}_{1}, \mathbf{r}_{2}), \tag{12}$$

where ψ_{bound} holds the information from the bound states of the target, n runs over all the bound states of the ion, and the coefficients $C(\mathbf{k}_n)$ and $C(\mathbf{k}_1, \mathbf{k}_2)$ are the amplitudes for single and double ionization channels, respectively. These amplitudes can be extracted using surface integrals involving $\Psi_{\text{sc}}^+(\mathbf{r}_1, \mathbf{r}_2)$ and the appropriate testing functions $\phi_{\mathbf{k}}(\mathbf{r})$ [31]. For double ionization, the amplitude is given by

$$C(\mathbf{k}_{1}, \mathbf{k}_{2}) = \frac{1}{2} e^{i\gamma} \int \{ \phi_{\mathbf{k}_{1}}^{-*}(\mathbf{r}_{1}) \phi_{\mathbf{k}_{2}}^{-*}(\mathbf{r}_{2}) \nabla \Psi_{\mathrm{sc}}^{+}(\mathbf{r}_{1}, \mathbf{r}_{2}) - \Psi_{\mathrm{sc}}^{+}(\mathbf{r}_{1}, \mathbf{r}_{2}) \nabla [\phi_{\mathbf{k}_{1}}^{-*}(\mathbf{r}_{1}) \phi_{\mathbf{k}_{2}}^{-*}(\mathbf{r}_{2})] \} \cdot d\mathbf{S}, \quad (13)$$

where γ is a volume-dependent phase that does not affect any physical observable [31]. The testing functions $\phi_{\mathbf{k}}$ above are chosen to be continuum solutions of the one-body Hamiltonian in Eq. (3) that asymptotically sees a nuclear charge of Z=2 for double ionization. By utilizing this choice of testing functions, we note that removal of all other components in Eq. (12) except those sought is accomplished by orthogonality. In all cases, correlation in the final state between the outgoing electrons is fully preserved in $\Psi_{\mathrm{sc}}^{+}(\mathbf{r}_{1}, \mathbf{r}_{2})$.

The generalized cross section for two photon double ionization process, within the framework of second-order time-dependent perturbation theory, can be formally written as [20,28,38]

$$\frac{d\sigma^{2\omega}}{dE_1 d\Omega_1 \Omega_2} = \frac{8\pi^3 (\Delta E_{fi}/2)^2 k_1 k_2}{c^2 E_0^4} \frac{|C(\mathbf{k}_1, \mathbf{k}_2)|^2}{|\tilde{\mathfrak{F}}(E_f, E_i, \omega, T)|^2}, \quad (14)$$

where the effective energy shape function for the radiation pulse, characterizing the particular energetic/temporal properties of the laser interaction is given by

$$\tilde{\mathfrak{F}}(E_f, E_i, \omega, T) = \frac{6e^{-izT}(e^{izT} - 1)\pi^4}{z^2[z^4T^4 - 20\pi^2z^2T^2 + 64\pi^4]},$$
 (15)

and where E_i is the energy of the initial state, $E_f \equiv E = k_1^2/2 + k_2^2/2$ is the energy of the final state, and $\Delta E_{fi} = E_f - E_i$, and $z = (2\omega - \Delta E_{if})$. A significant advantage in resolving the continuum dynamics utilizing the above expressions is that enables us, from a single time propagation, to extract the

generalized cross sections for any given final energy E within the bandwidth of the pulse.

C. Computational details

The ground state ${}^{1}S_{0}$ of Mg is determined by diagonalizing the field-free Hamiltonian constructed on a real radial grid up to $r_{\text{max}} = 50.0$ bohr. The orbital region, whose range is determined by the radial extent of the 1s, 2s and 2p orbitals in the core, was constructed within three finite elements with boundaries at 0.5, 8.0, and 16.0 bohr, and with 16th-order DVR in each. Such a dense grid, necessary to describe the core orbitals, produces high kinetic energy eigenvalues, resulting in very small time steps during the propagation. This issue is circumvented by removing these high eigenvalues for the propagation, allowing the use of bigger time steps and more compact grids without impacting any physical observable. The maximum single-electron angular momentum needed to converge the ground state energy and the TDCS that follow (in the energy range considered) was found to be $l_{\text{max}} = 7$. The time propagation was performed using a short-iterative Lanczos propagator [39–41] on a larger part of the grid up to $r_{\rm max} = 180$ bohr, with a time step $\Delta t = 1.25 \times 10^{-2}$ atomic units. Following the time propagation, the driven equation (Eq. 10) is then solved using an ECS contour beginning at $\mathcal{R}_0 = 180$ bohr (ECS angle $\theta = 30^\circ$) followed by three additional complex-scaled elements with boundaries at 188.0, 196.0, and 216 bohr. Finally, the results obtained using length gauge are practically identical to those obtained in the velocity gauge. Only length gauge results will be shown throughout.

III. RESULTS

In order to characterize the pathways towards the double continuum with respect to nonsequential versus sequential processes, we begin with an examination of the energy diagram of atomic magnesium shown in Fig. 1. Energies that follow are depicted relative to the double ionization continuum, which sets the zero point. In stark contrast to He, Mg has a very narrow energy region (less than 1 eV) where pure nonsequential double ionization can be observed. This is due to the fact that for Mg, the double ionization threshold E_0 itself is a few tens of eV (compared to He with $E_0 = -79$ eV) and, crucially, an intermediate state of the ion lies near the halfway point which bounds the nonsequential region from below (i.e., where $2\hbar\omega = E_0$). The nonsequential region is located just below the Mg⁺(3p) excited state, between $\hbar\omega = 11.4$ and 12.1 eV. Photons with an energy above $\hbar\omega = 12.1$ eV are sufficient to remove two electrons sequentially. This first sequential pathway is also substantially different than what occurs in helium: the sequential region for Mg first opens energetically via an excited state of Mg⁺, followed by the next sequential threshold that opens and leaves the cation of Mg^+ in the ground state configuration, $Mg^+(3s)$ (more analogous to the dominant helium pathway). Other nearby sequential thresholds for Mg are also shown in Fig. 1. It is important to note that these intermediate states of the Mg⁺ ion are relevant for sequential processes accessible at the photon energies considered here, while in contrast there is substantially more energetic spacing between the ground and

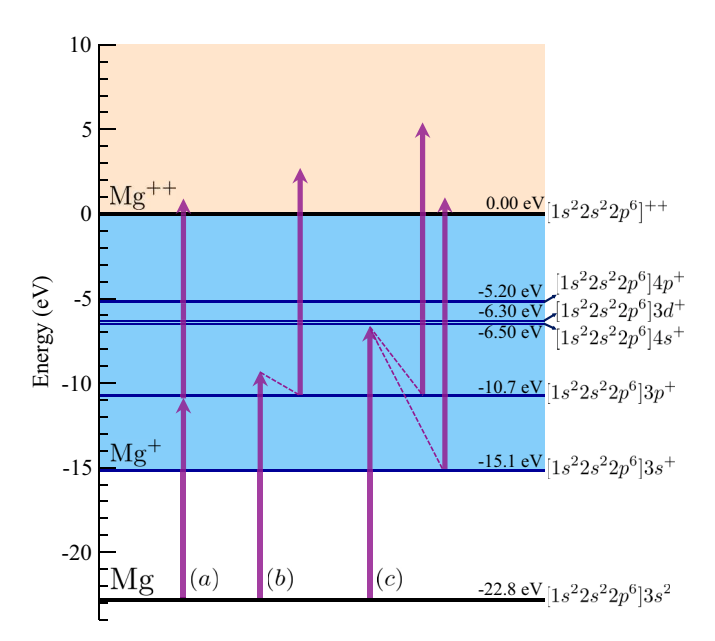


FIG. 1. Schematic representation of two-photon double ionization pathways for magnesium: (a) two-photon nonsequential double ionization, (b) two-photon sequential double ionization through the $\mathrm{Mg}^+(3p)$ state, and (c) two-photon sequential double ionization through the $\mathrm{Mg}^+(3p)$ and $\mathrm{Mg}^+(3s)$ states. The Mg and Mg^+ energy levels are shown within the frozen core approximation.

excited intermediate states of He⁺ that delineate the opening of the first and second sequential pathways.

We begin by examining the double ionization probabilities as a function of the energy sharing for two photon central frequencies. Figure 2 exhibits the single differential cross section (SDCS) for photons with a central frequency at $\hbar\omega=15.4~{\rm eV}$ (upper panel) and at $\hbar\omega=17.4~{\rm eV}$ (lower panel) for different pulse lengths. We note that, within the sequential region (which is applicable here throughout based on the very narrow nonsequential region and the finite bandwidth of the pulses considered), a cross section cannot be defined as the ratio of ionization rates to the photon flux; we instead refer to a "generalized" cross section [20,28,38], proportional to the square of the double ionization amplitude (with units as shown in the figures that follow) to report these probabilities and to be consistent with the nonsequential region where a cross section is well-defined.

Both panels of Fig. 2 exhibit substantial increases at near-equal energy sharings as the pulse length increases. Similar to what is observed for helium, the shortest pulse lengths reveal energy sharing probabilities that are relatively flat, possessing better correspondence with the energy-sharing behavior of one-photon double ionization processes at modest photon energies above the double ionization potential. Longer pulses reveal enhancement of the probability around pairs of peaks (due to the indistinguishability of the ionized electrons) that will begin to sharpen in the limit of infinite pulse lengths. In helium, however, the peaks are much better resolved by T=2.0 fs, and appear to onset as wings more towards unequal energy-sharing. By contrast, the results in magnesium display broad features that are not resolved at the longest pulse lengths shown. The intermediate ion states lying near

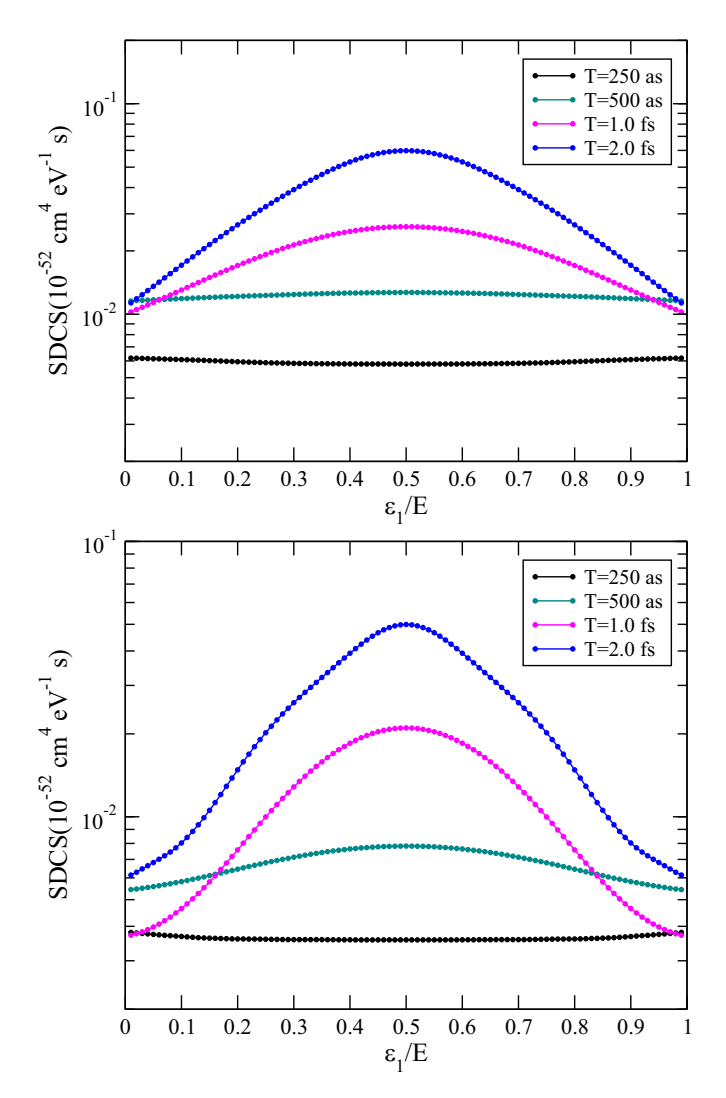


FIG. 2. Energy sharing (single differential) cross section results for double ionization of Mg at two central photon frequencies: $\hbar\omega=15.4$ (top) and 17.4 eV (bottom). Different pulse lengths are shown for each panel. Black points: 250 as pulse length. Dark-cyan points: 500 as pulse length. Magenta points: 1 fs pulse length. Blue points: 2 fs pulse length. Resonant peaks that appear near equal energy sharing for both photon energies in this sequential regime are broadened and unresolved for the longest pulses, while the shortest pulses shown exhibit a flatter response that is more indicative of single photon double ionization.

the midpoint of the energy level diagram in Fig. 1 for Mg make it so that substantially longer pulses would need to be used to resolve these features and distinguish the pairs of peaks that are accessed by (and concomitantly broadened by, as well) the finite pulse bandwidth. Solving the TDSE for such pulses would require the use of much larger radial grids, making the calculations extremely expensive. For the 2.0 fs pulse in the higher energy photon (lower) panel, the onset of new sequential pathways does begin to appear as shoulders further offset from the midpoint.

While the total ionization rates in the sequential region can be inferred from the energy sharing SDCS in Fig. 2, the opening of successive sequential pathways as the central frequency increases dramatically changes the angular distributions of

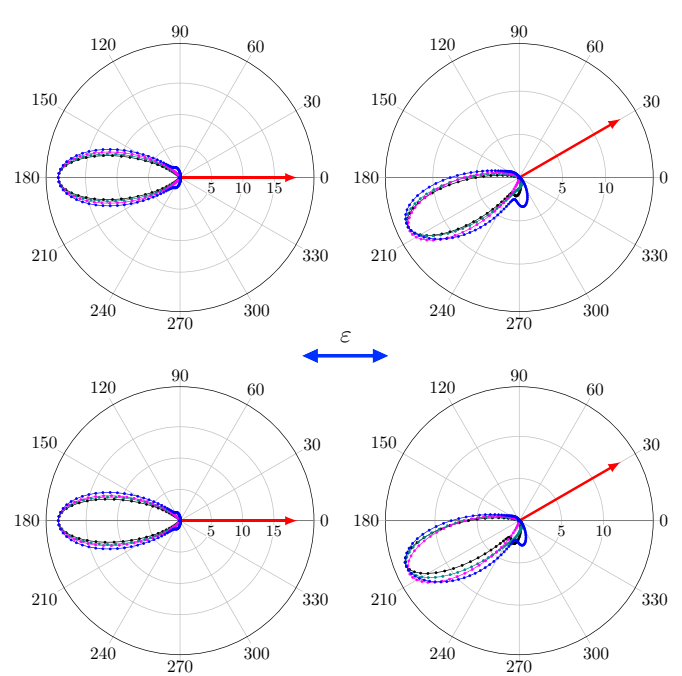


FIG. 3. TDCS at $\hbar\omega=11.9~\rm eV$ for double ionization of Mg for in-plane geometries. The central frequency of the photon is near the center of the narrow region of nonsequential ionization before sequential processes are open. The excess energy for the two electrons to share is 1 eV. Fixed electron (single ended red arrows) with 50% (upper row) and 90% (lower row) of the available energy and various directions with respect to the polarization (horizontal double ended blue arrow). Black points: 250 as pulse length. Dark-cyan points: 500 as pulse length. Magenta points: 1 fs pulse length. Blue points: 2 fs pulse length. Results have been normalized to largest magnitude cross section of the different pulse lengths for each energy sharing. Units are $10^{-55}~\rm cm^4~s~eV^{-1}~sr^{-2}$.

the electrons. We turn our attention to the (generalized) triple differential cross section (TDCS), defined in Eq. (14), and representing the most detailed information about the probabilities for two-photon double ionization that can be measured.

To first examine the narrow nonsequential regime, the TDCS at a central frequency of $\hbar\omega = 11.9$ eV are plotted in Fig. 3 for a variety of pulse durations. In the figures that follow, the TDCS of one electron is plotted in the plane containing the other electron fixed with respect to the linear polarization (co-planar geometry, $\phi_1 = \phi_2 = 0^\circ$). The fixed electron carries away 50% (upper row) and 90% (lower row) of the total available energy. Also, for the figures that follow, the pulse lengths in every panel range from 0.25 to 2.0 fs. The bandwidth (FWHM) of the intensity distribution in frequency of a \sin^2 pulse is $\Delta\omega \approx 2\pi/T$ with T denoting the full duration of the pulse, as in Eq.(9). So the widths of these pulses vary from 24.8 eV for 0.25 fs to 3.1 eV for a 1 fs pulse. For pulses at this photon energy (centering the pulse within the nonsequential region), the TDCS exhibits a highly correlated back-to-back emission relative to the fixed-electron direction for both angles considered (θ_1 at 0° or 30°), regardless of the pulse length and the energy sharing. We note that, for the pulse lengths considered, the bandwidth of the pulses is more than sufficient to extend into the sequential regime, yet the angular

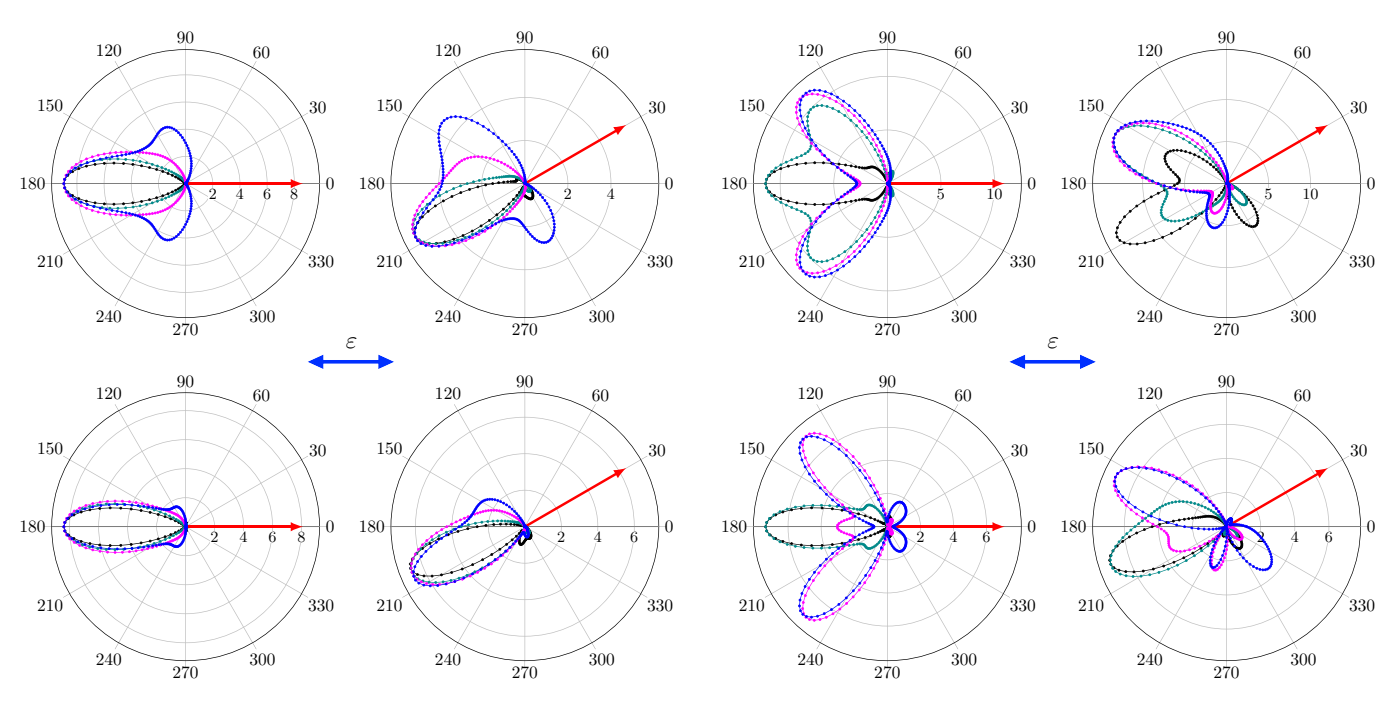


FIG. 4. Same as Fig. 3, but for photons of energy $\hbar\omega=13.4$ eV. At this photon central energy, sequential ionization is open only through the 3p excited state. The excess energy for the two electrons to share is 4 eV.

FIG. 5. Same as Fig. 3, but for photons of energy $\hbar\omega = 15.4$ eV. At this photon central energy, sequential ionization is open through the 3p excited state and the ground state 3s of the ion. The excess energy for the two electrons to share is 8 eV.

distributions appear to be more consistent with nonsequential double ionization. Additionally, the TDCS appear very similar for both energy sharings (upper and lower rows), exhibiting similar magnitudes and angular distributions. At this photon energy, the total energy shared between the electrons is small (about 1 eV), resulting in similar kinetic energies for the plotted electron, and thus producing similar features in the TDCS. These characteristics are consistent with previous DPI results obtained in He [2,6], where the temporal confinement of the two electron emission events is discussed in detail.

In the region between $\hbar\omega = 12.1$ and 15.1 eV the sequential ionization is open through only the $Mg^+(3p)$ excited state. Figure 4 shows the TDCS at a central frequency of $\hbar\omega = 13.4$ eV, again for different energy sharings (upper and lower rows) between the electrons. For the shorter pulses, nonsequential ionization features appear to dominate the cross section, manifesting as strongly back-to-back emission (as in Fig. 3). As the pulse length is increased, however, signatures of sequential ionization start to appear. For the longest pulse considered at T = 2.0 fs pulse duration, wings in the TDCS departing from the back-to-back direction become more prominent. Those wings are more pronounced at 50% energy sharing, while at 90% they appear as tiny features backgrounded upon the back-to-back dominant lobes. These secondary lobes in the angular distribution for the longest pulse lengths differ from the angular distributions seen in helium when first crossing into the sequential region. We note that the intermediate states that facilitate the first sequential region are distinct: here proceeding through the 3p state of the ion, while in helium the intermediate state is the ground state of the ion (1s). These orbitals are of different angular momentum and substantially different in radial character, the former possessing a radial node and larger extent. When both sequential and nonsequential channels are open, the contribution of the sequential channel in general becomes more important for longer pulses. In contrast to He where the sequential channel dominates for unequal energy sharing regardless the pulse duration, here the TDCS at 50% energy sharing shows more variation as a function of the pulse duration. The sequential peaks via the $\mathrm{Mg^+}(3p)$ intermediate state lie close to this energy sharing, thus we would expect a larger contribution from the sequential channel at these specific electron energies.

For photon energies higher than $\hbar\omega = 15.1$ eV, sequential ionization is open through the $Mg^+(3p)$ and $Mg^+(3s)$ states. Figure 5 shows the TDCS at a central frequency of $\hbar\omega = 15.4$ eV, again for different energy sharing between the electrons. As with the previous photon energy, for the shortest pulses considered here T = 250 as, nonsequential ionization dominates with back-to-back emission as the major feature for both energy sharings. For longer pulses, the small wings previously observed in the TDCS of Fig. 4 become more prominent, and more substantially so as the pulse length is increased. For both energy sharings plotted, the back-to-back structures that dominated the nonsequential and single openchannel sequential TDCS results have reversed in prominence with the secondary lobes of those previous cases at the longer pulse lengths. Examining the fast electron results for unequal energy sharing (lower rows) reveals additional small lobes closer in direction to the fixed electron and the variation of these structures depending on the energy sharing is dramatic.

The modification of the angular distribution patterns featuring increasingly complex structures for the same pulse lengths in the previous results as new sequential ionization pathways become energetically open is interesting to consider. In

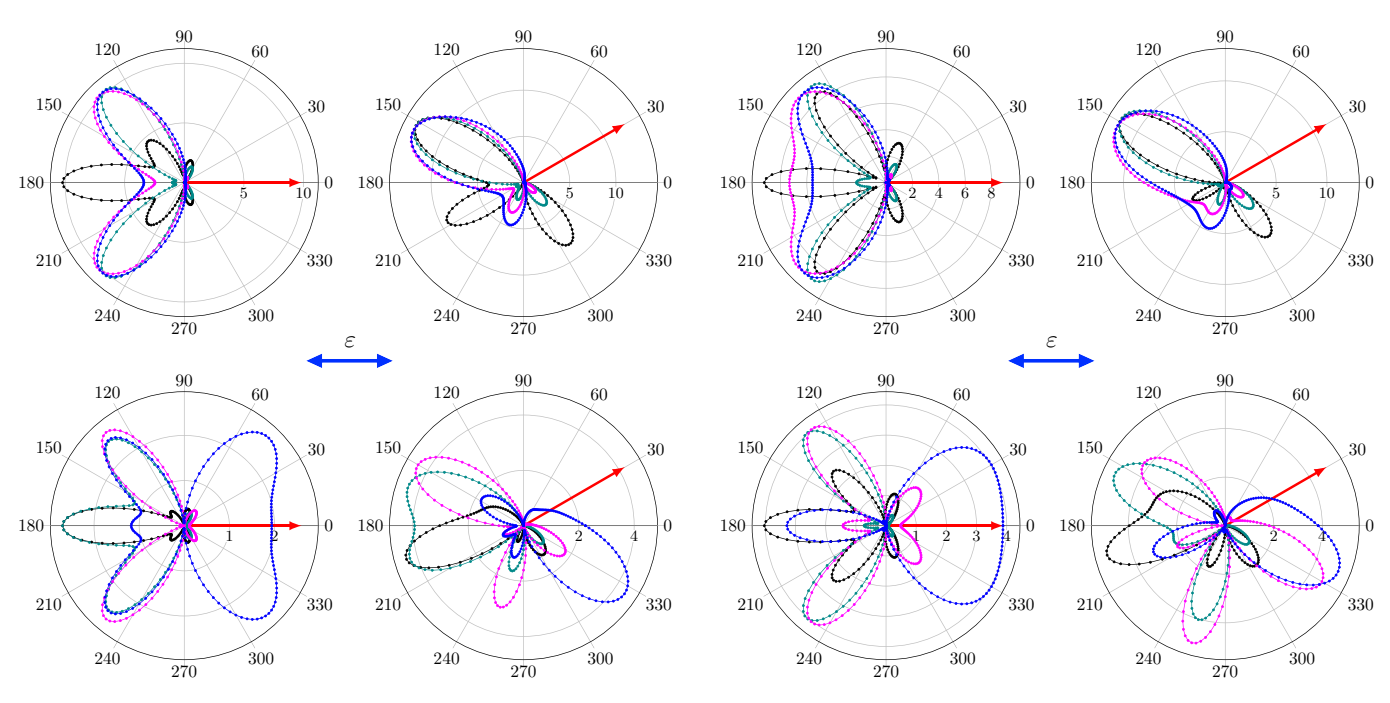


FIG. 6. Same as Fig. 3, but for photons of energy $\hbar\omega=16.4$ eV. In addition to those channels of the ion in Figs. 5 through which sequential ionization can proceed, the 4s intermediate state is accessible at this photon energy. The excess energy for the two electrons to share is 10 eV.

FIG. 7. Same as Fig. 3, but for photons of energy $\hbar\omega=17.4$ eV. In addition to those channels of the ion in Fig. 6 through which sequential ionization can proceed, the 3d intermediate state is accessible at this photon energy. The excess energy for the two electrons to share is 12 eV.

Figs. 6 and 7, we slightly increase the photon energy to $\hbar\omega =$ 16.4 and 17.4 eV, respectively. These increases correspond to photon energies where sequential ionization can proceed through additional intermediate states of the Mg⁺ ion: the 4s and 3d channels becoming energetically accessible, respectively. Although almost all the sequential ionization proceeds through the 3s and 3p channels, based on the dominance of these oscillator strengths [13], the dramatic variation of the angular distributions modified by the accessibility of these higher-lying excited state pathways is evident, and impacts the resulting angular distributions for even the shortest pulse lengths considered. To analyze this behavior and the striking evolution of the angular patterns as more nearby intermediatestate channels become accessible for a relatively narrow range of photon energies (and in contrast to helium, which requires more than a 1 eV of additional photon energy to access the next sequential threshold), we consider the importance of correlating configurations more necessary to accurately describe initial and final states in Mg relative to helium. A natural orbital decomposition of the initial state of these targets reveals the greater contribution of excited orbitals in correlating configurations. Specifically, for magnesium there are more prominent contributions from excited orbitals (3p, 4s, 3d, etc.)that are both energetically closer to the valence 3s orbital and also possess more complex nodal structure than is the case for helium, where the $1s^2$ configuration is substantially dominant and composed of orbitals that are largely separated energetically from the excited orbitals constituting the correlating configurations [42]. For the pulse lengths considered, the observed complicated angular distributions at these modest photon energies in Mg can be attributed to the greater

significance of the correlating contributions comprising the initial state, in addition to the fact that these excited contributions more prominently feature nearby orbitals that have a richer radial and angular structure than those which are analogous in correlating configurations of helium (2s, 2p, etc.).

IV. CONCLUDING REMARKS

We have presented energy- and angle-differential theoretical results for double ionization of the valence electrons of atomic magnesium by two-photon absorption. Very much in contrast to helium, a narrow range of less than 1 eV exists for magnesium where nonsequential ionization is the only allowed pathway due to the presence of intermediate states of the Mg^+ ion lying near the halfway point between the $3s^2$ valence state and the double ionization continuum. Examination of the angular distributions for different energy sharings and fixed electron directions reveals that sequential ionization effects dominate the TDCS at longer pulse lengths and that these angular patterns become more complex and less back-to-back from the fixed electron as the photon energy is modestly increased, due to additional open-channel sequential pathways that incorporate near-lying excited orbitals possessing a relatively high degree of radial and/or angular structure and which substantially contribute to correlating configurations. In general, the more the energies of the electrons sequentially ejected is made distinct, the less correlated (i.e., not back-to-back) the emission of the electrons appears across the various pulse lengths considered. The two-photon angular distributions in magnesium exhibit a substantial variation over relatively small increments in photon energy as additional sequential ionization thresholds are opened.

Comparisons of the TDCS results across different ns^2 targets reveals the effects of the different initial state environments for two-photon double ionization, as was also observed in the single-photon analog [18]. Although the overall symmetry of these processes, whether for one- or two-photon transitions, is the same for the heliumlike targets, the resulting angular distributions exhibit significant variation that highlights the nature of the correlating configurations underlying the configuration interaction representation of each target, as well as the individual structure of the orbitals that contribute to this expansion.

- J. Feist, S. Nagele, R. Pazourek, E. Persson, B. I. Schneider, L. A. Collins, and J. Burgdörfer, Phys. Rev. A 77, 043420 (2008).
- [2] R. Pazourek, J. Feist, S. Nagele, E. Persson, B. I. Schneider, L. A. Collins, and J. Burgdörfer, Phys. Rev. A 83, 053418 (2011).
- [3] M. Kurka, J. Feist, D. A. Horner, A. Rudenko, Y. H. Jiang, K. U. Kühnel, L. Foucar, T. N. Rescigno, C. W. McCurdy, R. Pazourek, S. Nagele, M. Schulz, O. Herrwerth, M. Lezius, M. F. Kling, M. Schöffler, A. Belkacem, S. Düsterer, R. Treusch, B. I. Schneider, L. A. Collins, J. Burgdörfer, C. D. Schröter, R. Moshammer, and J. Ullrich, New J. Phys. 12, 073035 (2010).
- [4] D. A. Horner, F. Morales, T. N. Rescigno, F. Martín, and C. W. McCurdy, Phys. Rev. A 76, 030701(R) (2007).
- [5] A. Palacios, T. N. Rescigno, and C. W. McCurdy, Phys. Rev. A 79, 033402 (2009).
- [6] F. Li, F. Jin, Y. Yang, J. Chen, Z.-C. Yan, X. Liu, and B. Wang, J. Phys. B: At., Mol. Opt. Phys. 52, 195601 (2019).
- [7] D. C. Griffin, M. S. Pindzola, C. P. Ballance, and J. Colgan, Phys. Rev. A 79, 023413 (2009).
- [8] M. W. McIntyre, A. J. Kinnen, and M. P. Scott, Phys. Rev. A 88, 053413 (2013).
- [9] M. S. Pindzola, C. P. Ballance, S. A. Abdel-Naby, F. Robicheaux, G. S. J. Armstrong, and J. Colgan, J. Phys. B: At., Mol. Opt. Phys. 46, 035201 (2013).
- [10] S. Laulan and H. Bachau, Phys. Rev. A 69, 033408 (2004).
- [11] S. A. Abdel-Naby, M. S. Pindzola, and J. Colgan, J. Phys. B: At., Mol. Opt. Phys. 48, 025204 (2015).
- [12] E. Sokell, P. Bolognesi, A. Kheifets, I. Bray, S. Safgren, and L. Avaldi, Phys. Rev. A 89, 013413 (2014).
- [13] D.-S. Kim and S. S. Tayal, J. Phys. B: At., Mol. Opt. Phys. 33, 3235 (2000).
- [14] G. Wang, J. Wan, and X. Zhou, J. Phys. B: At., Mol. Opt. Phys. 43, 035001 (2010).
- [15] R. Wehlitz, D. Lukić, and P. N. Juranić, J. Phys. B: At., Mol. Opt. Phys. 40, 2385 (2007).
- [16] G. Wang, J. Wan, and X. Zhou, Radiat. Phys. Chem. 130, 406 (2017).
- [17] E. Sokell, P. Bolognesi, A. Kheifets, I. Bray, S. Safgren, and L. Avaldi, Phys. Rev. Lett. 110, 083001 (2013).
- [18] F. L. Yip, T. N. Rescigno, and C. W. McCurdy, Phys. Rev. A 94, 063414 (2016).
- [19] L. A. A. Nikolopoulos, T. Nakajima, and P. Lambropoulos, Phys. Rev. Lett. 90, 043003 (2003).

ACKNOWLEDGMENTS

Work at LBNL was performed under the auspices of the US DOE under Contract DE-AC02-05CH11231 and was supported by the U.S. DOE Office of Basic Energy Sciences, Division of Chemical Sciences. Calculations presented here made use of the resources of the National Energy Research Scientific Computing Center, a DOE Office of Science User Facility. F.L.Y. was supported by the National Science Foundation, Grant No. PHY-1806417 and the U.S. DOE Office of Science, Office of Workforce Development for Teachers and Scientists (WTDS) under the Visiting Faculty Program.

- [20] A. Palacios, C. W. McCurdy, and T. N. Rescigno, Phys. Rev. A 76, 043420 (2007).
- [21] T. N. Rescigno and C. W. McCurdy, Phys. Rev. A 62, 032706 (2000)
- [22] F. L. Yip, C. W. McCurdy, and T. N. Rescigno, Phys. Rev. A 81, 053407 (2010).
- [23] F. L. Yip, C. W. McCurdy, and T. N. Rescigno, Phys. Rev. A 81, 063419 (2010).
- [24] F. L. Yip, F. Martín, C. W. McCurdy, and T. N. Rescigno, Phys. Rev. A 84, 053417 (2011).
- [25] F. L. Yip, A. Palacios, F. Martín, T. N. Rescigno, and C. W. McCurdy, Phys. Rev. A 92, 053404 (2015).
- [26] F. L. Yip, T. N. Rescigno, C. W. McCurdy, and F. Martín, Phys. Rev. Lett. 110, 173001 (2013).
- [27] F. L. Yip, A. Palaciosa, T. N. Rescigno, C. W. McCurdy, F. Martín, Chem. Phys. 414, 112 (2013), attosecond spectroscopy.
- [28] A. Palacios, T. N. Rescigno, and C. W. McCurdy, Phys. Rev. A 77, 032716 (2008).
- [29] A. Palacios, D. A. Horner, T. N. Rescigno, and C. W. McCurdy, J. Phys. B: At., Mol. Opt. Phys. 43, 194003 (2010).
- [30] L. Argenti, R. Pazourek, J. Feist, S. Nagele, M. Liertzer, E. Persson, J. Burgdörfer, and E. Lindroth, Phys. Rev. A 87, 053405 (2013).
- [31] C. W. McCurdy, M. Baertschy, and T. N. Rescigno, J. Phys. B: At., Mol. Opt. Phys. 37, R137 (2004).
- [32] C. W. McCurdy and F. Martín, J. Phys. B: At., Mol. Opt. Phys. **37**, 917 (2004).
- [33] B. Simon, Phys. Lett. A 71, 211 (1979).
- [34] C. A. Nicolaides and D. R. Beck, Phys. Lett. A 65, 11 (1978).
- [35] T. N. Rescigno, M. Baertschy, D. Byrum, and C. W. McCurdy, Phys. Rev. A 55, 4253 (1997).
- [36] B. Reps, W. Vanroose, and H. bin Zubair, J. Comput. Phys. 229, 8384 (2010).
- [37] A. Scrinzi, Phys. Rev. A 81, 053845 (2010).
- [38] L. A. A. Nikolopoulos and P. Lambropoulos, J. Phys. B: At., Mol. Opt. Phys. **34**, 545 (2001).
- [39] C. Leforestier, R. Bisseling, C. Cerjan, M. Feit, R. Friesner, A. Guldberg, A. Hammerich, G. J. d, W. Karrlein, H.-D. Meyer, N. Lipkin, O. Roncero, and R. Kosloff, J. Comput. Phys. 94, 59 (1991).
- [40] A. I. Kuleff, J. Breidbach, and L. S. Cederbaum, J. Chem. Phys. 123, 044111 (2005).
- [41] R. Kosloff, J. Phys. Chem. 92, 2087 (1988).
- [42] R. Y. Bello, F. L. Yip, T. N. Rescigno, R. R. Lucchese, and C. W. McCurdy, Phys. Rev. A 99, 013403 (2019).